MICROSTRUCTURE AND MECHANICAL PROPERTIES OF IN SITU AlB_2/A356 COMPOSITES UNDER T6 TREATMENT

Lei Jiao, BaoWang Wang, Yutao Zhao, Fan Li and ZhiWen Wang
School of Materials Science and Engineering, Jiangsu University, Zhenjiang 212013, China

Hui Li
School of Materials Science and Engineering, Jiangsu University of Science and Technology, Zhenjiang 212003, China

https://doi.org/10.1007/s40962-022-00828-3

Abstract

A new A356-KBF4 system was established, and AlB_2 particle-reinforced A356 composites were prepared by melt direct reaction method. The effects of AlB_2 particle content on the material structure and mechanical properties were investigated by scanning electron microscopy, microhardness, and room temperature tensile tests. The ultimate tensile strength of the AlB_2/A356 composite materials was increased by as much as 33% in the as-cast and 38% in the T6 conditions.

Keywords: *aluminum matrix composites, in situ synthesis, mechanical properties, AlB_2 particles, T6 treatment*

Introduction

A356 alloy is a high-strength aluminum alloy that can be heat-treated and strengthened. It has the advantages of excellent casting performance, high specific strength, corrosion resistance, and low cost. It has a wide range of applications in the aerospace field. However, because the coarse dendrites in A356 aluminum alloy affect its mechanical properties, grain refinement is an effective way to improve the properties of the alloy. At the same time, T6 treatment can also effectively improve the mechanical properties of A356 alloy.[1–6]

In the industrial preparation, TiB_2 refiner is prepared from Al-Ti-B by powder metallurgy to refine α-Al, but the addition of Ti will cause poisoning and weaken the properties of the alloy.[7–9] Agrawal et al.[10] studied the effect of magnetic stirring on the microstructure of the composite material during the melting and stirring process, and it was found that the magnetic field added to the dispersed TiB_2 particles also has a refinement effect on the α-Al grains, which has an effect on the hardness, tensile strength and dry slip resistance of the material. In addition, others refine α-Al by adding rare earth elements.[11,12] The addition of rare earth elements can not only refine grains but also replace iron in some Fe-containing brittle phases in aluminum alloys with rare earth elements. The performance improvement of aluminum alloy has a considerable impact.

Introducing enhanced particles in aluminum alloy is also a way to improve A356 alloy at present because the interface between the particles produced in situ and the aluminum matrix is clean and the bonding effect is good; the endogenous particles in situ are receiving more and more attention.[13–18] The preparation of α-Al refiner particles by in-situ reaction has become a feasible and effective way of grain refinement. Jinhua Ding[19] used melt spinning technology and ultrasonic vibration technology to successfully prepare NdB6 nanoparticle-reinforced Al-Cu-Mn alloy in situ so that NdB_6 particles are uniformly dispersed in the matrix alloy, and there is good wettability between the particles and the aluminum. When the alloy is observed using polarized light, the α-Al crystal grains have changed from coarse dendrites to fine equiaxed crystals, and the effect of refining is significant. The Al-Ti-C[20–22] system also has a very significant effect as a refiner. Chezheng Cao et al.[23] used Al-K_2TiF_6-C (diamond) to successfully generate TiC nanoparticles in situ, but the study found that the wettability between C and Al is not sufficient and the C

Received: 02 March 2022 / Accepted: 19 May 2022 /
Published online: 4 July 2022

becomes oxidized. Chen Gang[24] et al. tried to add kaolin ($Al_2O_3{\cdot}2SiO_2{\cdot}2H_2O$) to the aluminum liquid in the semi-solid state of A356 to generate γ-Al_2O_3 particles by in-situ reaction and calculated the mismatch with α-Al by TEM analysis. γ-Al_2O_3 also has the effect of refining α-Al grains.

On the other hand, T6 treatment (solution treatment + artificial aging) of A356 aluminum alloy can also greatly improve the mechanical properties of the material.[25–30] I. Chakrabarty[31] et al. found that T6 treatment can break the as-cast eutectic silicon dendrites and spheroidize the broken eutectic silicon dendrites. The coarse eutectic silicon is transformed into fine spherical particles, which improves the tensile strength and ductility of the material. All have been significantly improved and are expected to meet the basic requirements of automobile cylinder liners.

Among many in-situ reinforcement particles, AlB_2 particles are used as effective nucleation sites for aluminum alloys.[32,33] Linlin Yuan et al.[34] prepared AlB_2/A356 composites by powder metallurgy and studied their friction and wear behavior. Few studies on α-Al grain refinement and alloy mechanical properties in in situ synthesized composites. In this study, the in-situ AlB_2 particle-reinforced A356 aluminum alloy composite was prepared by developing a new A356-KBF_4 system and subjected to T6 treatment. Analyze its microstructure to study its mechanical properties.

Materials and Methods

Preparation for Composites

The raw materials used to prepare xwt% AlB_2/A356 (x = 2; 4; 6; 8) composite materials are industrial A356 alloy ingots (see Table 1 for composition) and inorganic salt KBF_4 powder. The KBF_4 powder was dried at 250 °C for 2.5 hours. The mold is preheated at 200 °C for half an hour. Melting of A356 alloy ingots at 870 °C using a high-frequency induction furnace, and then add KBF_4 powder. To avoid flotation, graphite clocks can be used to press inorganic salts into the melt. At the same time, the magnetic field is turned on, and the inorganic salt and the melt are reacted for 30 minutes at a magnetic field frequency of 10 Hz. After the reaction, the melt is refined and the slag is removed. After cooling the melt to 720 °C, it was poured into a copper mold with dimensions of 100 × 20 × 200 mm and obtain an ingot-like xwt% AlB2/A356 (x = 2;4;6;8) composite material, then processed into tensile specimens. (gauge length:15, thickness:2mm, width:4mm).

Hardness Testing

The hardness sample is processed into a cube of 10 mm×10 mm×10 mm by the SYJ-400 metallographic cutting machine. Use KB30S hardness tester to perform hardness test under 1N and formula (1), test each sample 10 times, and take the average value to obtain the Vickers hardness of the material.

$$\mathrm{HV} = 0.102 \times \frac{F}{S} = 0.012 \times \frac{2F\sin\frac{\alpha}{2}}{d^2} \qquad \text{Eqn. 1}$$

T6 Treatment

T6 treatment on the material under the condition of

(1) The solution temperature is set to 540 °C and the temperature of the samples is kept for 6h, then they are quenched in 50 °C water. Experimental equipment: KSL-1200X heat treatment furnace.
(2) The artificial aging temperature was set at 170 °C, and the test time was 15 hours, microhardness was measured every hour after quenching in water at 30 °C.

Mechanical Performance Test

The Instron-5569 universal tensile testing machine was used to conduct tensile tests on tensile specimens with a gauge length of 15×5×2 mm^3 at a constant tensile rate of 0.5 mm/min. Each material is subjected to three tensile tests and the average value is taken to obtain the tensile properties of the material. The true stress, true strain, and work hardening rate are calculated by formula (2, 3, and 4).

$$\sigma_{\mathrm{true}} = \sigma_{\mathrm{eng}} * \left(1 + \varepsilon_{\mathrm{eng}}\right) \qquad \text{Eqn. 2}$$

$$\varepsilon_{\mathrm{true}} = \ln\left(\varepsilon_{\mathrm{eng}} + 1\right) \qquad \text{Eqn. 3}$$

$$n = \frac{\mathrm{d}(\ln \sigma_{\mathrm{true}})}{\mathrm{d}(\ln \varepsilon_{\mathrm{true}})} \qquad \text{Eqn. 4}$$

Table 1. Ingredients of A356 Alloy Ingots

Elements	Si	Mg	Ti	Fe	Mn	Cu	Zn	Sn	Pb	Al
Percentage	7.39	0.37	0.15	<0.16	<0.10	<0.05	<0.05	<0.01	<0.03	balance

Characterization

SEM and metallographic samples were ground with 2000-grit sandpaper and then polished on a polishing machine, and then the microstructure was observed. Analysis of materials by means of characterization instruments: X-ray diffraction (XRD, BRUKER D8 ADVANCE XRD, Germany), polarizing microscope (PC, LEICA ICC50 W, Germany), scanning electron microscope (SEM, Carl Zeiss Merlin Compact, Germany) and an energy dispersive spectrometer (EDS). The size of α-Al grains is measured by image pro plus software.

Results and Discussions

Phase Analysis

It can be clearly seen from Figure 1 that the XRD pattern of xwt % AlB_2/A356 composite shows the diffraction peak of AlB_2.In contrast, the XRD pattern of A356 does not show the diffraction peak of AlB_2, indicating that AlB_2 particles have been successfully synthesized. By searching the literature,[35] it is determined that the reaction equation of AlB_2 is Formula 5

$$2KBF4 + 3Al = AlB2 + 2KAlF4 \qquad \text{Eqn. 5}$$

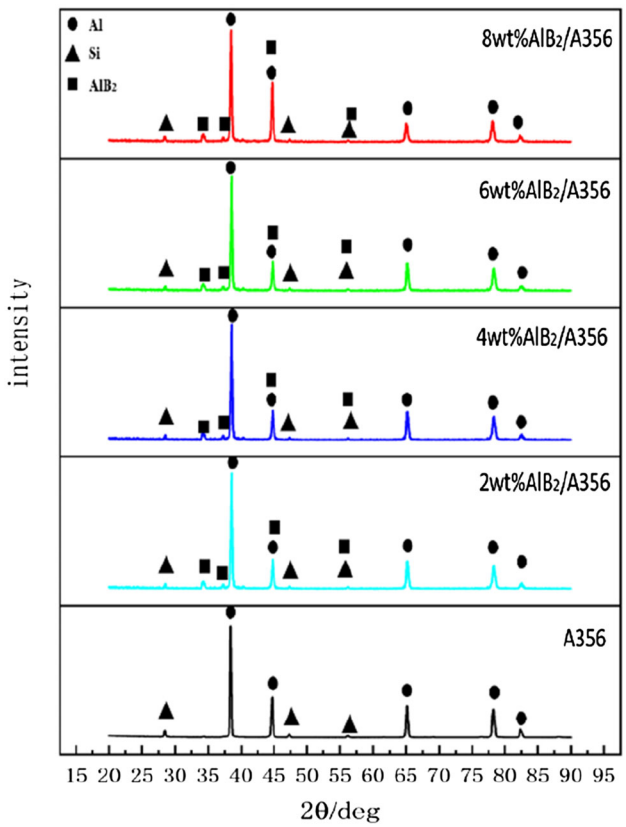

Figure 1. XRD pattern of xwt%AlB_2/A356(x = 2, 4, 6, 8).

The plane spacing between AlB_2 and Al is obtained by MDI Jade 6 software. According to formula (6), the mismatch between AlB_2 and Al matrix is calculated to be 3.76%, indicating that AlB_2 particles have a specific refining effect on Al grains.

$$\delta_{(hkl)_n}^{(hkl)_s} = \frac{1}{3}\sum_{i=1}^{3}\frac{|d(uvw)_s^i \cos\theta - d\ (uvw)_n^i|}{d(uvw)_n^i} \times 100\% \qquad \text{Eqn. 6}$$

Microstructure Morphology

Enhanced Particle Distribution

Figure 2 is the SEM image of different materials. The EDS spectrum and atomic content of the particles are shown in Figure 2 and Table 2. EDS analysis of the particles shows that there are only two characteristic peaks of Al and B elements in the particles. The characteristic peak of AlB2 appeared in the XRD analysis, so it can be inferred that the particles are AlB2 particles generated in situ. It can be seen from Figure 2 that when the AlB_2 particle content is 2wt% and 4wt%, the AlB_2 particles are more dispersed but the number is smaller. AlB_2 particles are hexagonal, which is consistent with the hexagonal lattice of AlB_2. When the particle content increases to 6wt%, it can be clearly seen that the particles have a tendency to agglomerate and the shape of the particles has many rectangular particles in addition to the hexagonal shape.

Grain Size Analysis

Figures 3 and 4 are the polarized light micrographs and α-Al grain size distribution diagrams of A356 alloy matrix and AlB_2 particles reinforced A356 composites with different mass fractions. It can be seen from Figure 4(a) and (e) that with the increase of the mass fraction of AlB_2 particles, the size of the α-Al grains continues to decrease. When the mass fraction of AlB_2 particles reaches 6wt%, the α-Al grains reach the minimum value. However, when the mass fraction of AlB_2 particles reaches 8wt%, the refining effect of the reinforcing particles on the α-Al grains fails. This may be due to the excessive aggregation of the particles after the excessive particle content, and the AlB_2 particles that can be used as the core of the heterogeneous nucleation are reduced.

Hardness

Figure 5 shows the Vickers hardness diagram of A356 alloy and A356 composites reinforced with different AlB_2 particles content. The standard deviation is shown in Figure 5 in the form of error bars. It can be seen from Figure 5 that the change trend of the Vickers microhardness of A356

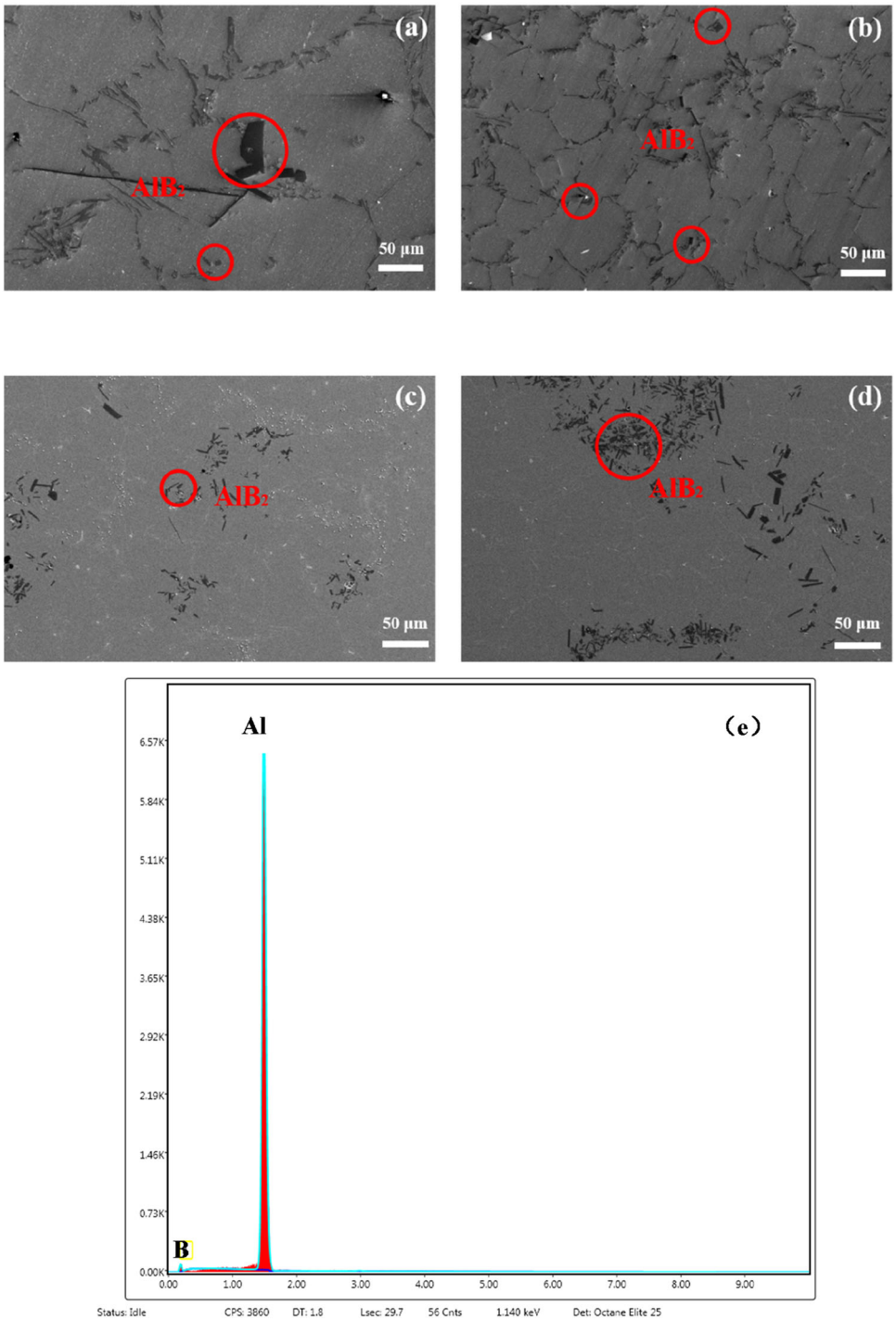

Figure 2. SEM and EDS images of the A356 matrix composites reinforced by different content of AlB_2 particles: (a):2wt% (b):4wt% (c):6wt% (d):8wt% (e): EDS spectrum of AlB_2.

Table 2. The Amount of Al and B

Element	Weight%	Atomic%
B	22.13	41.49
Al	77.87	58.51

matrix and composite materials is inversely proportional to the α-Al grain size in the material. This phenomenon is basically consistent with the Hall-Petch formula in the micron scale, which represents these refined grains have more grain boundaries per unit area, and shear deformation occurs in adjacent grains. A sufficient stress concentration must be generated at the grain boundaries. Refining grains can produce more grain boundaries. If the grain boundary

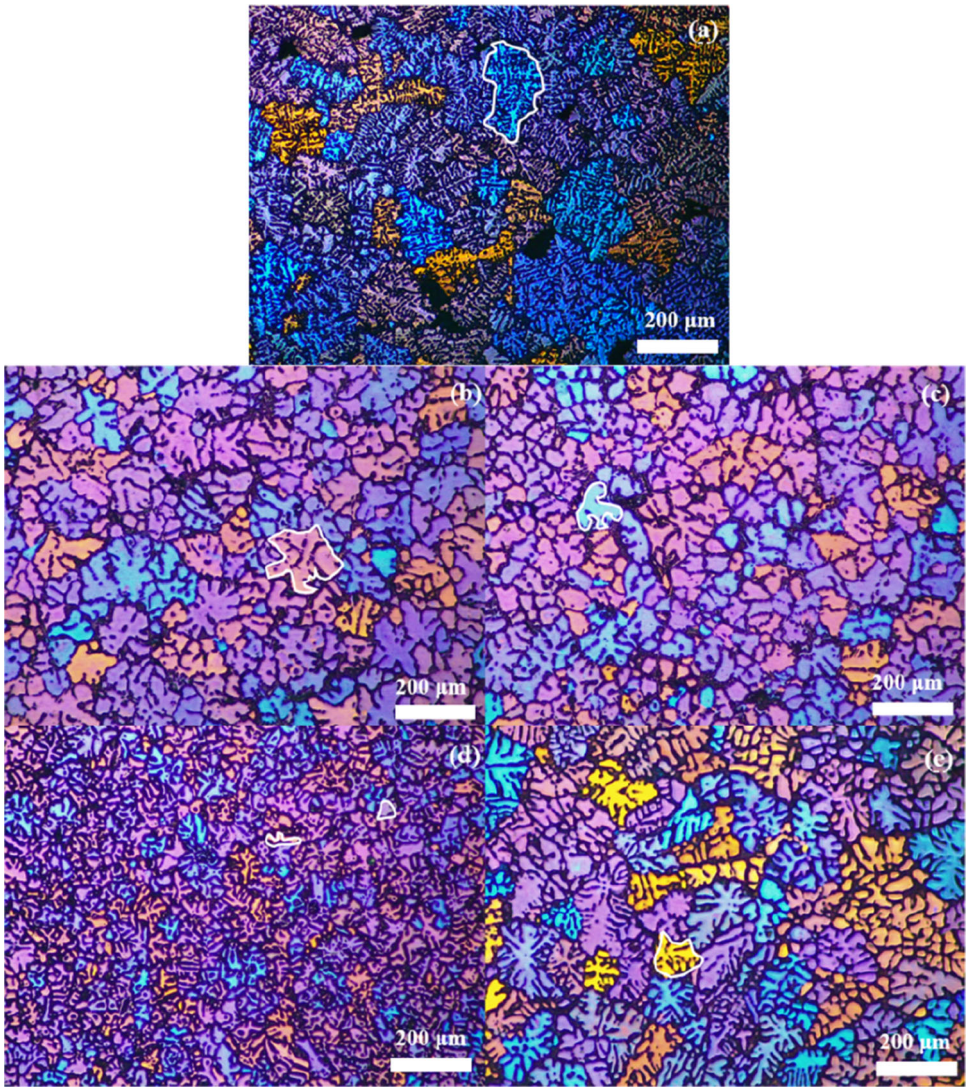

Figure 3. PC images of the A356 matrix composites reinforced by different content of AlB_2 particles: (a):A356 (b): 2wt% (c): 4wt% (d): 6wt% (e): 8wt%.

structure does not change, a greater external force is required to generate dislocation plugging and strengthen the material.

T6 Treatment

Figure 6 is the metallographic diagram of A356 alloy, A356-T6 alloy, and 6wt.% AlB_2/A356-T6 composite. It can be seen from the figure that Si mainly exists in the shape of chaotic needles in the A356 alloy. T6 treatment can first dissolve the second phase and solute atoms into the alloy through the solid solution process to homogenize and make Si spheroidized, and secondly, the second phase in the supersaturated state is precipitated through the aging process, and the precipitated second phase The dislocation pinning can effectively improve the properties of the alloy. It can also be seen from the figure that the microstructure of the A356 alloy treated by T6 is reduced and the distribution of needle-like substances is more uniform. However, needle-like Si can hardly be seen in the metallographic diagram of the T6-treated composite, which may be because the addition of dual-phase particles has a limiting effect on the growth of Si. The spheroidization of Si phase can reduce the brittle phase in the alloy and enhance the mechanical properties of the material.

Mechanical Properties

Figure 7 is the tensile curve of the matrix and the composite material with different AlB_2 content and the ultimate tensile strength, yield strength, and elongation of these materials are shown in Table 3. It can be seen from Figure 7 and Table 3 that the addition of AlB_2 particles has an optimizing effect on the mechanical properties of the material. When the mass fraction of AlB_2 reaches 6wt%, the ultimate tensile strength of the material is increased by

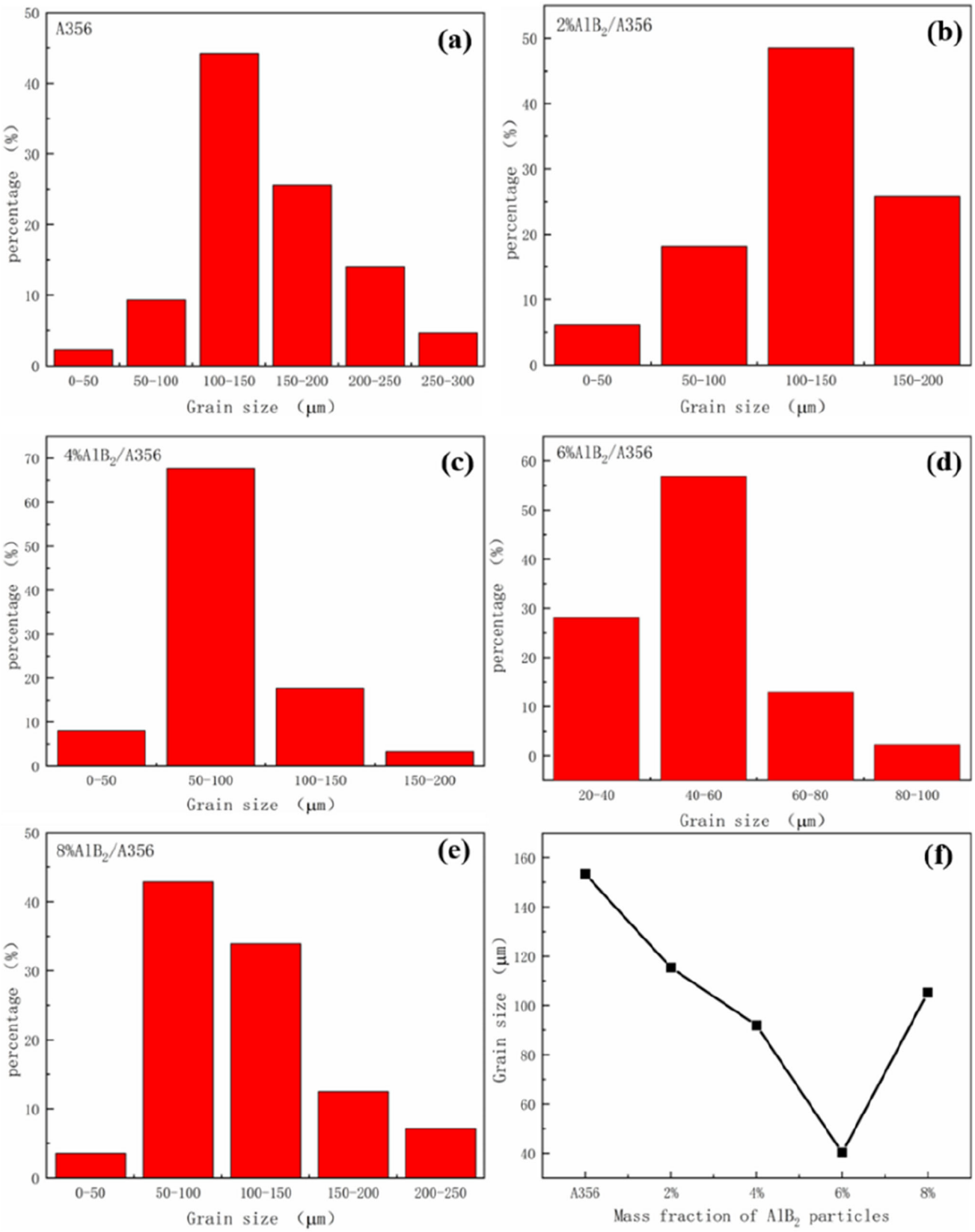

Figure 4. Grain size of the A356 matrix composites reinforced by different content of AlB_2 particles: (a):A356 (b): 2wt% (c): 4wt% (d): 6wt% (e): 8wt% (f): average size.

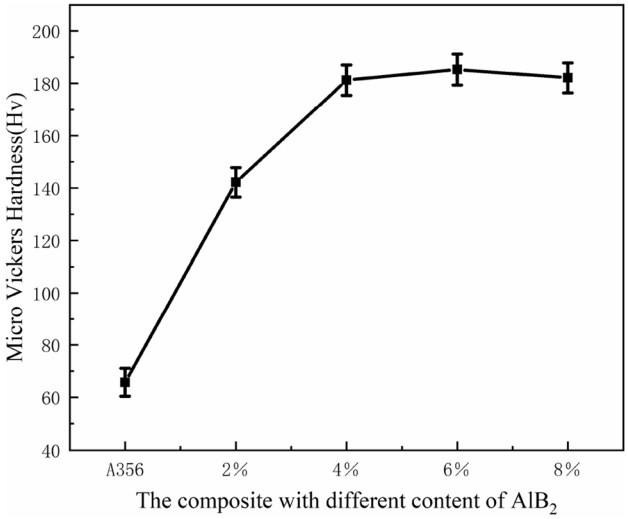

Figure 5. The Micro Vickers Hardness of the matrix and the xwt%/A356 composite.

33.2% relative to that of the A356 matrix, and the elongation of 6wt%AlB_2/A356 composite material reached 18.12%. This may be caused by the refining effect of AlB_2 on α-Al grains. The fine grains undergo plastic deformation by external force and can be dispersed in more grains, the plastic deformation is more uniform, and the stress concentration is smaller; the finer the grains, the larger the area of the grain boundary; the more tortuous the grain boundary, the less conducive to the propagation of cracks. On the other hand, the true stress and true strain values of the material are calculated by the tensile curve and the $\ln\sigma_{true}$-$\ln\varepsilon_{true}$ curve is drawn (Figure 8). Through the analysis of the figure, the work hardening index (n) of the material is obtained. The n value of the A356 base alloy is 0.104. When the AlB_2 particle content in the A356 alloy reaches 6wt%, the n value reaches 0.253. The increase in the n value represents the increase in the forming limit of the material. The material can bear more at the moment when the material shrinks stress, which may be another reason for the increase in the tensile strength of the material.

Figure 9 is the peak aging diagram of T6 treatment of different materials. From the figure, it can be clearly found that the hardness of cast aluminum alloy-A356 is

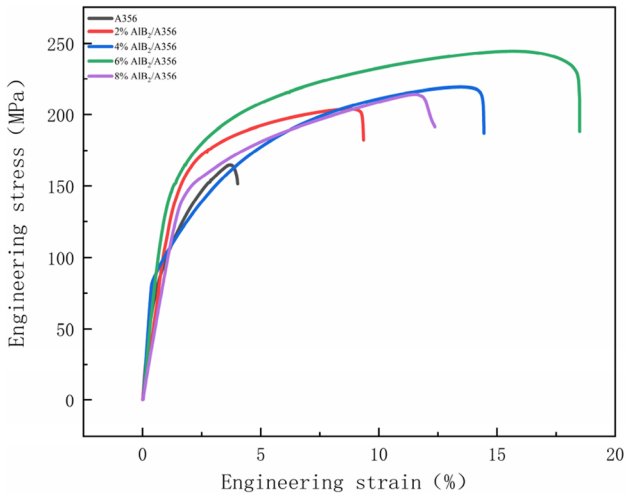

Figure 7. Engineering stress-engineering strain curves of different materials.

Table 3. The Ultimate Tensile Strength (UTS), Yield Strength (YS), and Elongation (%) of Different Materials-as-Cast Condition

Materials	Ultimate tensile strength (MPa)	Yield strength (MPa)	Elongation (%)
A356	158.8 + 3	75.3 + 2	4.3 + 0.2
2wt%AlB_2/A356	187.3 + 4	127.4 + 3	8.7 + 0.4
4wt%AlB_2/A356	192.6 + 3	130.5 + 3	14.2 + 0.3
6wt%AlB_2/A356	211.6 + 2	152.2 + 4	18.1 + 0.2
8wt%AlB_2/A356	191.5 + 3	129.6 + 3	13.0 + 0.5

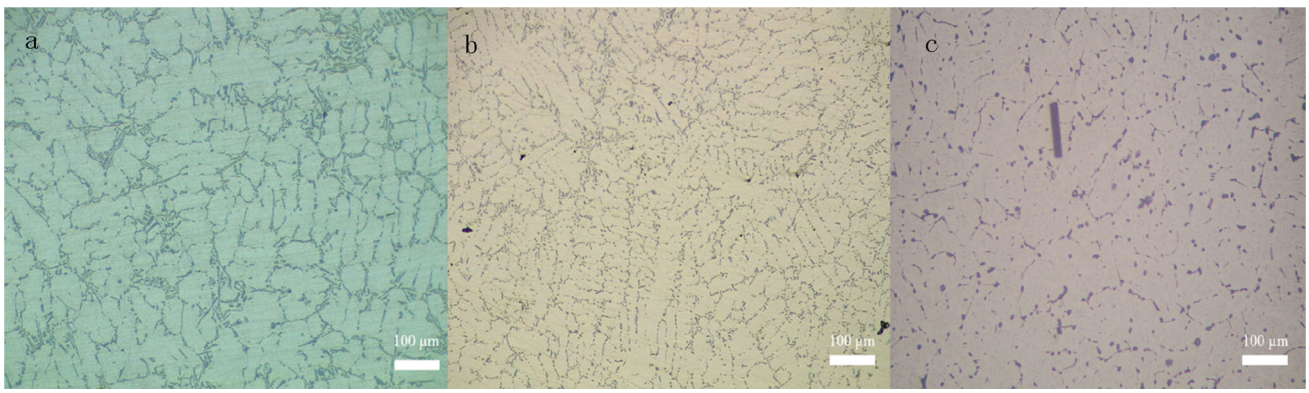

Figure 6. Metallographic images of A356 alloy, A356-T6 alloy, and 6wt.%AlB_2A356-T6 composite (a): A356 (b): A356-T6 (c): 6wt.%AlB_2A356-T6 composite.

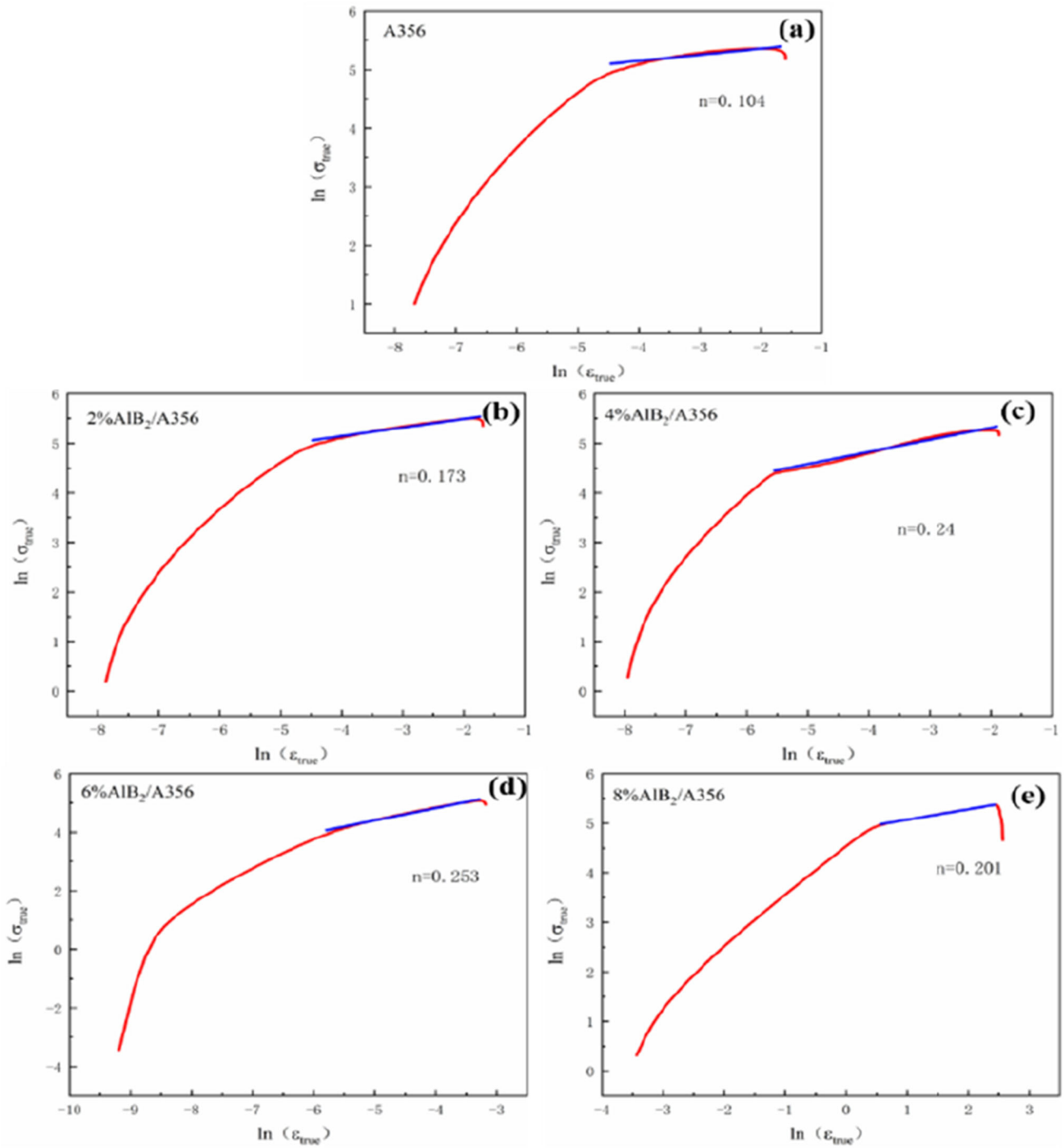

Figure 8. $\ln\sigma_{true}$-$\ln\varepsilon_{true}$ curves of different materials.

significantly improved by T6 treatment. The time to peak for different materials is 8h (A356), 10 h (2wt%AlB2/A356), 11h (4wt%AlB_2/A356), 11 h (6wt%AlB_2/A356), 12 h (8wt%AlB_2/A356). By comparing the peak time of different materials, it can be seen that the peak time of the material increases with the increase of AlB_2 content, which may be because some particles at the grain boundary hinder the precipitation of precipitates during artificial aging, prolonging the artificial aging time.

Figure 10 shows the tensile curves of composites with different AlB2 contents and A356 matrix after T6 treatment. The ultimate tensile strength, yield strength, and elongation of these materials are shown in Table 4. From the comparison of Tables 3 and 4, it can be seen that the T6 treatment significantly improves the tensile properties of the material. When the mass fraction of AlB_2 reaches 6wt%, the ultimate tensile strength is increased by 45.02% compared with the material without T6 treatment. This is

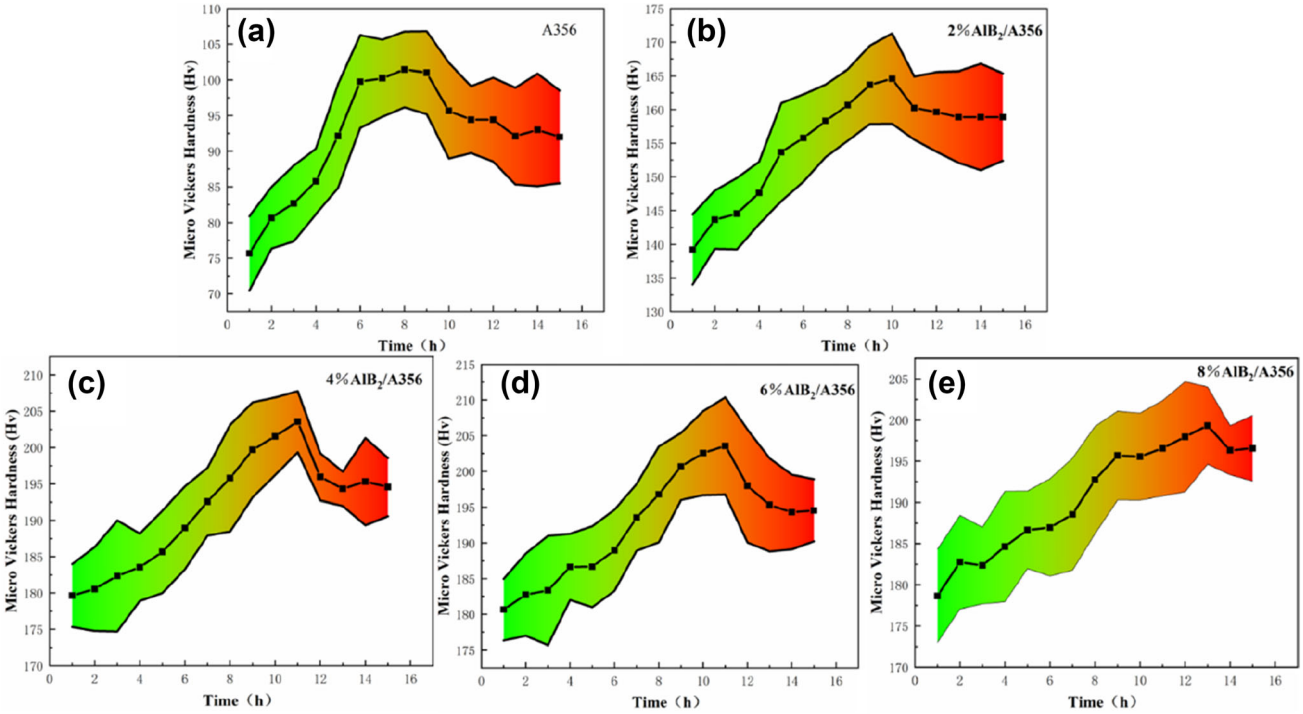

Figure 9. Aging peak graph for different materials.

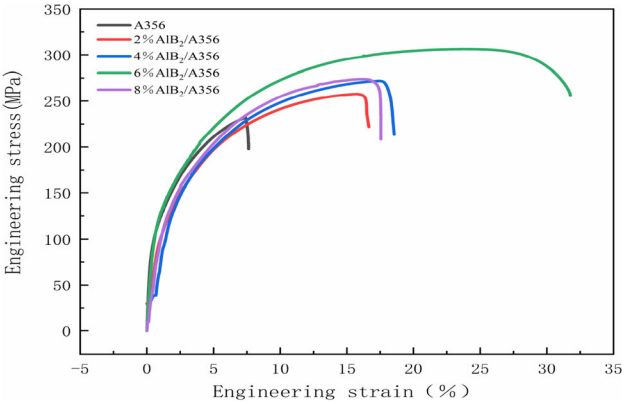

Figure 10. Engineering stress-engineering strain curves of different materials under T6 at 8h (A356), 10 h (2wt%AlB2/A356), 11h (4wt%AlB_2/A356), 11 h (6wt%AlB_2/A356), 12 h (8wt%AlB_2/A356).

because some disperse phases in the total A356 after T6 treatment turn from metastable to stable state and these disperse phases are more uniformly distributed through the process of solid solution to reprecipitation. On the other hand, the true stress and true strain values of the material are calculated from the tensile curve, and the $\ln\sigma_{true}$-$\ln\varepsilon_{true}$ curve is drawn in Figure 10. Through the analysis of the graph, the work hardening index (n) of the material is obtained. The n value of A356-T6 of 0.362 is much higher than that of the A356 alloy without T6 treatment (Figure 11). When the content of AlB_2 particles in A356 alloy reaches 6wt %, after T6 treatment, the n value reaches 0.414. An increase in the value of n represents an increase

Table 4. The Ultimate Tensile Strength (UTS), Yield Strength (YS) and Elongation (%) of Different Materials Under T6 at 8h (A356), 10 h (2wt%AlB_2/A356), 11h (4wt%AlB_2/A356), 11 h (6wt%AlB_2/A356), 12 h (8wt%AlB_2/A356)

Materials	Ultimate tensile strength (MPa)	Yield strength (MPa)	Elongation (%)
A356	221.31 + 2	125.67 + 2	7.3 + 0.2
2wt%AlB_2/A356	257.64 + 3	146.23 + 3	15.53 + 0.4
4wt%AlB_2/A356	271.96 + 2	157.82 + 2	18.56 + 0.3
6wt%AlB_2/A356	306.32 + 4	168.96 + 4	23.26 + 0.2
8wt%AlB_2/A356	273.80 + 3	152.32 + 2	17.23 + 0.5

in the forming limit of the material. The moment the material shrinks, the material can withstand more stress, which may be another reason for the increased tensile strength of the material.

Figure 12 is a SEM image of the tensile fracture of A356, A356-T6, and 6wt % AlB2/A356-T6. It can be seen from the figure that the fracture mode of A356 alloy is mainly brittle fracture, and there are only some small dimples in the fracture morphology. The fracture mode of the A356 alloy after T6 treatment is still brittle fracture, but the

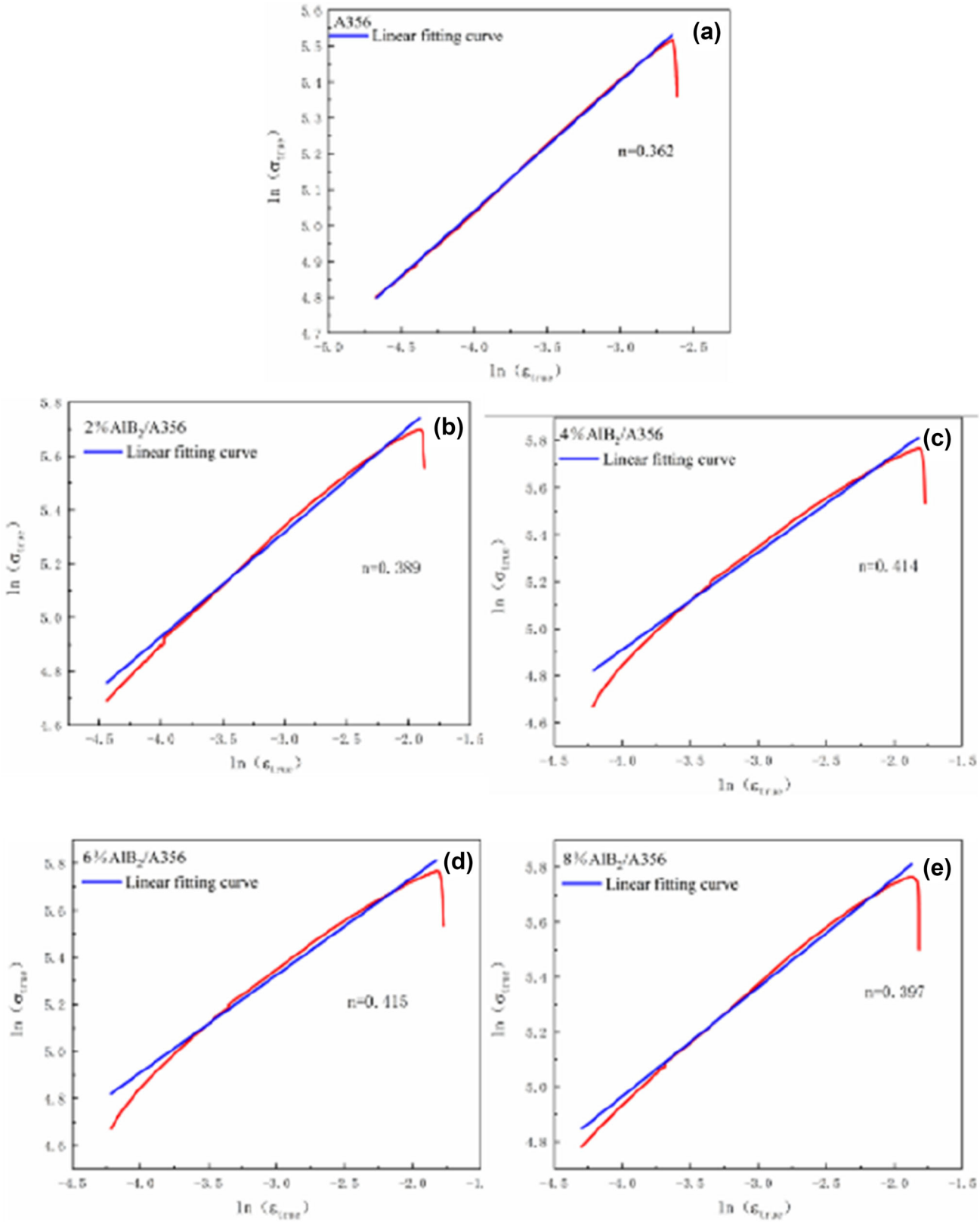

Figure 11. $\ln\sigma_{true}$-$\ln\varepsilon_{true}$ curves of different materials under T6 at 8h (A356), 10 h (2wt%AlB2/A356), 11h (4wt%AlB_2/A356), 11 h (6wt%AlB_2/A356), 12 h (8wt%AlB_2/A356).

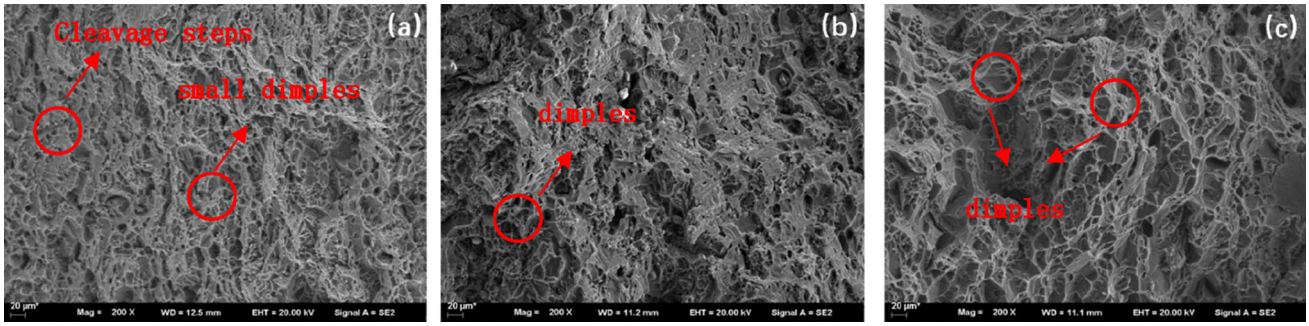

Figure 12. SEM of tensile fracture of different materials (a):A356 (b):A356-T6 (c):6%AlB_2/A356-T6.

dimples in the fracture morphology become larger, indicating that the toughness has been improved to a certain extent, which is consistent with the data shown by the tensile curve. There are a large number of large dimples in the tensile fracture morphology of 6wt %AlB_2/A356 composite after T6 treatment, indicating that the fracture form of 6wt %AlB_2/A356 composite is ductile fracture. This is due to the combined effect of the addition of AlB2 particles and the strengthening of the matrix by T6 treatment.

Conclusion

The AlB_2 particle-reinforced A356 composite material with different mass fractions was obtained by the melt direct reaction method, and the following conclusions were obtained:

(1) Phase analysis by XRD and microstructure observation by SEM proved that the A356-KBF_4 system can prepare AlB_2 reinforced A356 composites. Polarized observation of different materials found that the addition of AlB_2 has a refinement effect on the α-Al grains.

(2) In the study of the as-cast material, it was found that the hardness test and room temperature tensile results show that the addition of AlB_2 particles can significantly improve the mechanical properties of the material. When the content of AlB_2 particles reaches 6wt%, the microhardness and tensile strength of the material reach the maximum value of 180.8 Hv and 211.6 MPa. In addition, the elongation of the material is also significantly improved due to the refinement of α-Al by the addition of AlB2 particles.

(3) The mechanical properties of the T6-state materials were tested and found that the mechanical properties of all the tested materials were significantly improved after T6 treatment. The ultimate tensile strength of the 6wt% AlB2/A356 composite increased by 38.5%, and the fracture mode was ductile fracture. The presence of particles inhibits the precipitation of the precipitated phase during artificial aging, resulting in a longer time to reach the aging peak with increasing particle content.

Acknowledgement

This research was financially supported by the (1) National Natural Science Foundation of China, No. U20A20274. (2) National Natural Science Foundation of China, No. 52071158. (3) National Natural Science Foundation of China, No. U1664254. (4) Innovation Fund of Industrial Center of Jiangsu University, No.ZXJG2020062.

REFERENCES

1. M.S. Ashok Kumar, C. Honnaiaha, S.L. Ajit Prasad, Influence of extrusion process on mechanical and tribological properties of aluminium A356–AL2O3 stir cast MMC[J]. Mater. Today Proc. **5**(13), 26918–26924 (2018)
2. G. Li, W. Jiang, F. Guan et al. Improving mechanical properties of AZ91D magnesium/A356 aluminum bimetal prepared by compound casting via a high velocity oxygen fuel sprayed Ni coating[J]. J. Magnes. Alloys, 2021
3. S.R. Sagar, K.M. Srikanth, R. Jayasimha, Effect of cryogenic treatment and heat treatment on mechanical and tribological properties of A356 reinforced with SiC[J]. Mater. Today Proc. **45**, 184–190 (2021)
4. G. Sigworth, Understanding quality in aluminum castings. Inter. J. Metalcast. **5**, 7–22 (2011). https://doi.org/10.1007/BF03355504
5. G.K. Sigworth, T.A. Kuhn, Grain refinement of aluminum casting alloys. Inter. J. Metalcast. **1**, 31–40 (2007). https://doi.org/10.1007/BF03355416
6. G.K. Sigworth, The modification of AI-SI casting alloys: important practical and theoretical aspects. Inter. J. Metalcast. **2**, 19–40 (2008). https://doi.org/10.1007/BF03355425
7. B.-X. Dong, Q. Li, Z.-F. Wang, et al. Enhancing strength-ductility synergy and mechanisms of Al-based composites by size-tunable in-situ TiB2

particles with specific spatial distribution[J]. Compos. Part B Eng. 2021
8. L.-L. Zhang, H.-X. Jiang, J. He et al., Kinetic behaviour of TiB2 particles in Al melt and their effect on grain refinement of aluminium alloys[J]. Trans. Nonferrous Metals Soc. China **30**(8), 2035–2044 (2020)
9. J. Sun, X.-Q. Wang, Y. Chen et al., Effect of Cu element on morphology of TiB2 particles in TiB2/Al−Cu composites[J]. Trans. Nonferrous Metals Soc. China **30**(5), 1148–1156 (2020)
10. S. Agrawal, A.K. Ghose, I. Chakrabarty, Effect of rotary electromagnetic stirring during solidification of In-situ Al-TiB2 composites[J]. Mater. Des. **113**, 195–206 (2017)
11. W. Ding, X. Zhao, T. Chen et al., Effect of rare earth Y and Al–Ti–B master alloy on the microstructure and mechanical properties of 6063 aluminum alloy[J]. J. Alloys Compounds **830**, 154685 (2020)
12. J. Zhang, C. Su, X. Chen et al., First-principles study on pitting corrosion of Al deoxidation stainless steel with rare earth element (La) treatment[J]. Mater. Today Commun. **27**, 102204 (2021)
13. S. Sardar, I. Roy, S. Chakraborty et al., A selective approach towards synthesis of poly (3-bromo thiophene)/graphene quantum dot composites via in-situ and ex-situ routes: application in light emission and photocurrent generation[J]. Electrochim. Acta **365**, 137369 (2020)
14. M.H. Daneshifar, A. Papi, M. Alishahi, Fabrication of Al-Si/Mg2Si in-situ composite by friction stir processing[J]. Mater. Lett. **282**, 128832 (2021)
15. R. Wang, W. Guo, J. Wang et al., Effects of stress state, strain rate, and temperature on fracture behavior of in situ TiB2/2024 Al composite[J]. Mech. Mater. **151**, 103641 (2020)
16. B. Guo, M. Song, X. Zhang et al., Achieving high combination of strength and ductility of Al matrix composite via in-situ formed Ti-Al3Ti core-shell particle[J]. Mater. Charact. **170**, 110666 (2020)
17. B. Shi, S. Huang, P. Zhu et al., In-situ TiN reinforced composite coatings prepared by plasma spray welding on Ti6Al4V[J]. Mater. Lett. **276**, 128093 (2020)
18. H. Li, S. Lu, P. Xu et al., Microstructure and tribological properties of in-situ formed Al3Zr/A356 composite[J]. Mater. Res. Express **7**(5), 056510 (2020)
19. J. Ding, C. Cui, Y. Sun et al., Preparation of in-situ NdB6 nanoparticles and their reinforcement effect on Al–Cu–Mn alloy[J]. J. Alloy. Compd. **806**, 393–400 (2019)
20. Y. Dong, M. Wang, G. Zhang et al., Influence of Ti/C mass ratio on the microstructure of Al-Ti-C master alloy and refinement effect on pure aluminum[J]. Results Phys. **23**, 104000 (2021)
21. L. Zhao, F. Zhang, L. Wang et al., Effects of post-annealing on microstructure and mechanical properties of plasma sprayed Ti-Si-C composite coatings with Al addition[J]. Surf. Coat. Technol. **416**, 127164 (2021)
22. T. Gao, S. Zhang, G. Liu et al., A high strength AlSi10Mg alloy fabricated by laser powder bed fusion with addition of Al–Ti–C–B master alloy powders[J]. Materialia **16**, 101103 (2021)
23. C. Cao, H. Ling, N. Murali et al., In-situ molten salt reaction and incorporation of small (10 nm) TiC nanoparticles into Al[J]. Materialia **7**, 100425 (2019)
24. J. Xu, G. Chen, Z. Zhang et al., Effect of Al-3 wt% Al2O3 master alloy fabricated by calcined kaolin on grain refinement and mechanical properties of A356 alloy[J]. J. Alloys Compounds **862**, 158512 (2021)
25. S.L. Pramod, A.K. Prasada Rao et al., Microstructure and mechanical properties of as-cast and T6 treated Sc modified A356–5TiB2 in-situ composite[J]. Mater. Sci. Eng. A **739**, 383–394 (2019)
26. T. Haskel, G.O. Verran, R. Barbieri, Rotating and bending fatigue behavior of A356 aluminum alloy: effects of strontium addition and T6 heat treatment[J]. Int. J. Fatigue **114**, 1–10 (2018)
27. R. Gecu, S. Acar, A. Kisasoz et al., Influence of T6 heat treatment on A356 and A380 aluminium alloys manufactured by thixoforging combined with low superheat casting[J]. Trans. Nonferrous Metals Soc. China **28**(3), 385–392 (2018)
28. M.I. Houria, Y. Nadot, R. Fathallah et al., Through process Modeling applied to the fatigue design of cast A356–T6 components[J]. Eng. Fract. Mech. **195**, 267–278 (2018)
29. S.L. Pramod, A.K.P. Rao et al., Effect of Sc addition and T6 aging treatment on the microstructure modification and mechanical properties of A356 alloy[J]. Mater. Sci. Eng. A **674**, 438–450 (2016)
30. Y.-C. Duan, F.-F. Zhang, D. Yao et al., Numerical prediction of fatigue life of an A356–T6 alloy wheel considering the influence of casting defect and mean stress[J]. Eng. Fail. Anal. **118**, 104903 (2020)
31. S.C. Ram, K. Chattopadhyay, I. Chakrabarty, Microstructures and high temperature mechanical properties of A356-Mg2Si functionally graded composites in as-cast and artificially aged (T6) conditions[J]. J. Alloy. Compd. **805**, 454–470 (2019)
32. A.E. Steinman, S. Corthay, K.L. Firestein et al., Al-based composites reinforced with AlB2, AlN and BN phases: experimental and theoretical studies[J]. Mater. Des. **141**, 88–98 (2018)
33. S. Koksal, F. Ficici, R. Kayikci et al., Experimental optimization of dry sliding wear behavior of in situ AlB2/Al composite based on Taguchi's method[J]. Mater. Des. **42**, 124–130 (2012)
34. L. Yuan, J. Han, J. Liu et al., Mechanical properties and tribological behavior of aluminum matrix composites reinforced with in-situ AlB2 particles[J]. Tribol. Int. **98**, 41–47 (2016)

35. X. Kai, S. Huang, L. Wu et al., High strength and high creep resistant ZrB2/Al nanocomposites fabricated by ultrasonic-chemical in-situ reaction[J]. J. Mater. Sci. Technol. **35**(9), 2107–2114 (2019)